

# X-Ray Nanothermometry of Nanoparticles in Tumor-Mimicking Tissues under Photothermia

Rosalía López-Méndez, Javier Reguera, Alexandre Fromain, Esraa Samy Abu Serea, Eva Céspedes, Francisco Jose Teran, Fangyuan Zheng, Ana Parente, Miguel Ángel García, Emiliano Fonda, Julio Camarero, Claire Wilhelm, Álvaro Muñoz-Noval,\* and Ana Espinosa\*

Temperature plays a critical role in regulating body mechanisms and indicating inflammatory processes. Local temperature increments above 42 °C are shown to kill cancer cells in tumor tissue, leading to the development of nanoparticle-mediated thermo-therapeutic strategies for fighting oncological diseases. Remarkably, these therapeutic effects can occur without macroscopic temperature rise, suggesting localized nanoparticle heating, and minimizing side effects on healthy tissues. Nanothermometry has received considerable attention as a means of developing nanothermosensing approaches to monitor the temperature at the core of nanoparticle atoms inside cells. In this study, a label-free, direct, and universal nanoscale thermometry is proposed to monitor the thermal processes of nanoparticles under photoexcitation in the tumor environment. Gold-iron oxide nanohybrids are utilized as multifunctional photothermal agents internalized in a 3D tumor model of glioblastoma that mimics the *in vivo* scenario. The local temperature under near-infrared photo-excitation is monitored by X-ray absorption spectroscopy (XAS) at the Au L<sub>3</sub>-edge (11 919 eV) to obtain their temperature in cells, deepening the knowledge of nanothermal tumor treatments. This nanothermometric approach demonstrates its potential in detecting high nanothermal changes in tumor-mimicking tissues. It offers a notable advantage by enabling thermal sensing of any element, effectively transforming any material into a nanothermometer within biological environments.


## 1. Introduction

Body temperature and its regulation are crucial for most vital functions and metabolic processes.<sup>[1]</sup> It is also an indicator of tissue homeostasis.<sup>[2]</sup> Treatment of many diseases can benefit from therapeutic effects that take place by locally controlling temperature in tissues such as bacterial or virus infection, diabetes, inflammation of tissues, and cancer. Indeed, an increase in temperature in tumor tissues (from 41 to 42 °C), that is, hyperthermia, is used as an adjuvant anticancer treatment in clinical settings in combination with radiation and/or radiotherapy.<sup>[3]</sup> The progress of nanotechnology in medicine has revolutionized hyperthermia methods by providing highly localized heating through the activation of nanomaterials by means of external magnetic fields<sup>[4]</sup> (magnetic hyperthermia) or near-infrared (NIR) light<sup>[5]</sup> (photothermia) with successful tumor reduction.

Local temperature monitoring during hyperthermia treatments is essential to avoid undesired cytotoxic effects and to preserve healthy tissues. Moreover, the use of moderated temperatures or even macroscopic

R. López-Méndez, F. J. Teran, J. Camarero, A. Espinosa  
IMDEA Nanociencia  
c/ Faraday, 9, Madrid 28049, Spain  
E-mail: ana.espinosa@csic.es

J. Reguera, E. S. A. Serea, F. Zheng  
BCMaterials  
Basque Center for Materials  
Applications and Nanostructures  
UPV/EHU Science Park  
48940 Leioa, Spain  
A. Fromain, C. Wilhelm  
Laboratoire Physico Chimie Curie  
PCC  
CNRS UMR168  
Institut Curie, Sorbonne University  
PSL University  
Paris 75005, France  
E. Céspedes, A. Espinosa  
Instituto de Ciencia de Materiales de Madrid  
ICMM-CSIC  
Madrid 28049, Spain

 The ORCID identification number(s) for the author(s) of this article can be found under <https://doi.org/10.1002/adhm.202301863>

© 2023 The Authors. Advanced Healthcare Materials published by Wiley-VCH GmbH. This is an open access article under the terms of the Creative Commons Attribution-NonCommercial-NoDerivs License, which permits use and distribution in any medium, provided the original work is properly cited, the use is non-commercial and no modifications or adaptations are made.

DOI: 10.1002/adhm.202301863

athermal conditions has demonstrated therapeutic effects triggered by induced hot-spot regions instead of global macroscopic heating.<sup>[6]</sup> In hyperthermia experiments, most of the thermometry approaches are based on non-contact techniques, aiming for minimally invasive probe systems. However, those traditional thermometers cannot accomplish other multiple requirements that should be simultaneously satisfied to be used as thermal sensors in cells and tissues, including i) high spatial resolution, ii) high temperature sensitivity, and iii) robustness against fluctuation in the biological environments (unconstrained of pH, ionic strength, or cell type). Nanothermometers based on luminescent nanoparticles,<sup>[7]</sup> fluorescent organic dyes,<sup>[8]</sup> quantum dots,<sup>[9]</sup> nanodiamonds,<sup>[10]</sup> thermosensitive polymers,<sup>[11]</sup> and metallic nanoparticles<sup>[12]</sup> have fulfilled these requisites by providing very precise temperature readouts within tissues<sup>[13]</sup> or even being used as intracellular temperature probes<sup>[14,15]</sup> for thermogenic processes or thermal treatments. All these thermal nanoprobe have been selected to be reliable at the physiological conditions in terms of temperature range (20–80 °C) and high wavelength optical performance (excitation/emission operatives in the biological windows).<sup>[16]</sup> Besides the materials used, techniques such as Raman spectroscopy,<sup>[17]</sup> X-ray diffraction,<sup>[18]</sup> magnetic resonance,<sup>[19]</sup> or hyperspectral photoluminescence confocal image<sup>[20]</sup> have been also used as nanoscale thermometric approaches. Recently, we explored an in situ and direct nanothermometric method based on the measurement of structural parameters of nanomaterials under photothermal conditions using X-ray absorption spectroscopy (XAS).<sup>[21]</sup> The validity of the method was demonstrated in plasmonic-based single (Au nanorods) and hybrid (Au/Fe<sub>3</sub>O<sub>4</sub>) nanomaterials under thermal laser exposure that display excellent thermo-therapeutic performance,<sup>[22,23]</sup> where considerable nanothermal gradients were detected. The advantages of this methodological approach are essentially threefold: i) it is based on an element-sensitive technique, which does not require the design of extra nanosensors to provide precise nanoscale temperature readings, allowing a universal thermal probe methodology as any material can turn into a nanothermometer, ii) it provides an interatomic thermal resolution specifically sensing the released heat at the heart of thermoactivated cores, and iii) it can operate over a wide range

of temperatures, procuring a robust and reliable tool to explore potentially sharp thermal gradients.

The present study represents a significant achievement in advancing this X-ray-based nanothermometric methodology, pushing the frontiers even further into the cellular scenario. This work consists in applying this unique label-free and direct nanoscale thermometry to monitor the thermal processes of nanoparticles under photoexcitation in the tumor environment while simultaneously mitigating any potential damage to healthy cells caused by excessive heating. To achieve this, we have evaluated the local temperature induced in gold-iron oxide nanomaterials (Au/Fe<sub>3</sub>O<sub>4</sub>) in tumor cells under NIR photothermal protocols by means of analyzing the EXAFS signal at the Au L<sub>3</sub>-edge. We have developed 3D cell culture models of glioblastoma, organized as spheroids to mimic more accurately the tumor structure<sup>[24]</sup> and encapsulating cells having internalized Au/Fe<sub>3</sub>O<sub>4</sub>, in order to evaluate both global and nanoscale photo-induced temperatures achieved inside cells forming a tissue. An exceptional advantage of this method lies in its universal and versatile nature, allowing any element to be excited and serve as a nanothermometer in biological environments.

## 2. Results

### 2.1. Gold and Iron-Oxide Nanohybrids in 3D Tumor Spheroids

The selected nanomaterials are hybrid nanostructures that combine magnetic and plasmonic features as this combination presents a high degree of multifunctionality.<sup>[25]</sup> More specially, the ones selected here have a Janus-type structure composed of a branched gold side and an iron oxide nanosphere side, which exhibit excellent heating properties,<sup>[22]</sup> easy functionalization,<sup>[26]</sup> and multimodal imaging capabilities.<sup>[23]</sup> They have also been proven as efficient magnetically guided photothermal agents for in vivo applications.<sup>[22]</sup> The Au/Fe<sub>3</sub>O<sub>4</sub> nanohybrids were synthesized by a multistep seed-mediated-growth method to produce nanoparticles with a 20 nm-iron oxide core decorated with Au spikes in a ratio [Au]/[Fe] = 1.6 (see transmission electron microscopy (TEM) micrographs in **Figure 1A**) with a 34 ± 4 nm average equivalent diameter (**Figure S1**, Supporting Information). The generated nanohybrids were coated by PVP (polyvinylpyrrolidone polymer) that guaranteed high colloidal stability in water and buffers, because of its steric and coulombic stability ( $\zeta = -10$  mV at pH 7).<sup>[27]</sup>

The photo-activated thermal capabilities of Au/Fe<sub>3</sub>O<sub>4</sub> nanohybrids (when irradiated in the NIR region) have been previously explored in tumor cells with outstanding therapeutic outcomes.<sup>[22]</sup> To study the local temperature at the nanoscale in the tumor environment, we have focused on a 3D spheroid glioblastoma (U87 human cell line) tumor cell model. Spheroid models resemble tumoroids and are used to mimic solid tumors hence their biological complexity promotes the production of extracellular matrix (ECM) and enhances the cell-cell interaction and cell packaging.<sup>[28]</sup> These factors are important to evaluate the induced thermal effect generated with nanomaterials from within the cancer cells in a realistic tumor mass, their consequent heat exchange, and losses with the environment. U87 glioblastoma cells have been proven as optimal candidates to form cohesive multicellular tumor spheroids, showing dense cell contact,

A. Parente, Á. Muñoz-Noval  
Dpto. Física Materiales  
Facultad CC. Físicas  
Universidad Complutense de Madrid  
Madrid 28040, Spain  
E-mail: almuno06@ucm.es  
M. Á. García  
Departamento de Electrocerámica  
Instituto de Cerámica y Vidrio  
ICV-CSIC  
Kelsen 5, Madrid 28049, Spain  
E. Fonda  
Synchrotron SOLEIL  
L'Orme des Merisiers – St. Aubin-BP 48, Gif/s/ Yvette 91192, France  
J. Camarero  
Departamento de Física de la Materia Condensada and Instituto 'Nicolás Cabrera'  
Universidad Autónoma de Madrid  
Madrid 28049, Spain

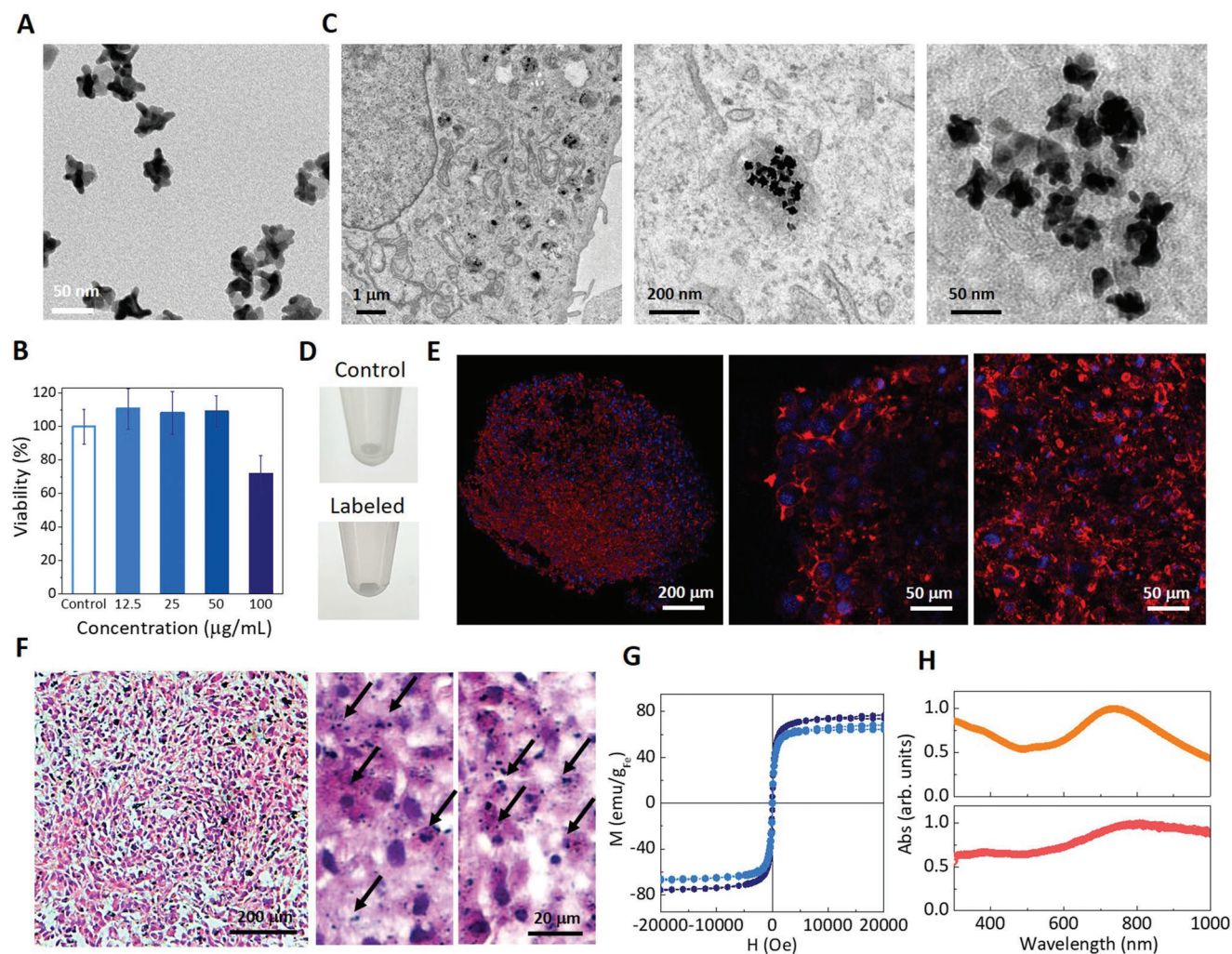


**Figure 1.** Gold iron-oxide hybrids as magneto-photothermal agents in 3D tumor spheroids. A) TEM images of synthesized gold-iron oxide nano hybrids. B) Cell viability of gold-iron oxide nano hybrids in U87 glioblastoma cells incubated at 12.5, 25, 50, and 100  $\mu\text{g}_{\text{TOTAL}} \text{mL}^{-1}$  for 24 h internalized in U87 cells ( $n = 3$ ). C) TEM micrographs of gold-iron oxide nano hybrids in U87 cells. Nano hybrids are inside endosomal compartments. D) Images of control and labeled (with nano hybrids) spheroids. E) Confocal images of a spheroid stained with actin (cytoskeleton, red) and with DAPI (nucleus, blue) at different orientation planes: 3D reconstruction (left), plane bottom (central), and border surface (right) of the spheroid. F) Spheroid section stained with hematoxylin/eosin (viable cells in pink, nucleus in purple, and extracellular matrix in light pink). G) Magnetization hysteresis loop at 300 K of  $\text{Au}/\text{Fe}_3\text{O}_4$  synthesized nano hybrids (dark blue) and in cells (light blue). H) UV-vis-NIR spectra of previous samples in solution (on top) and in cells (down), which display a plasmon resonance at the NIR region.

rounded morphologies, and viable cores. Cell viability treated with different concentrations of nano hybrids was beforehand analyzed in 2D cell culture models (25–100  $\mu\text{g}_{\text{TOTAL}} \text{mL}^{-1}$ , where  $\text{g}_{\text{TOTAL}}$  is the total mass of Au and  $\text{Fe}_3\text{O}_4$  elements). Biocompatibility was satisfactory at doses lower than 100  $\mu\text{g}_{\text{TOTAL}} \text{mL}^{-1}$  (Figure 1B).

The nano hybrids were then incubated for 24 h at an extracellular Au concentration of  $[\text{Au}] = 50 \text{ to } 200 \times 10^{-6} \text{ M}$  (lower than 50  $\mu\text{g}_{\text{TOTAL}} \text{mL}^{-1}$ ). Nano hybrids were easily uptaken by cells (with Fe content ranging from 3.2 to 8.6 pg per cell and Au content ranging from 4.0 to 19.5 pg per cell at these incubation conditions, see Figure S2 (Supporting Information and Experimental Section) and internalized in endosomal compartments as shown in TEM micrographs (Figure 1C; Figure S3, Supporting Informa-

tion). Nano materials morphology was not altered by the exposure to the cellular environment, maintaining intact their star-like architecture of Au bound to the iron oxide lobes and invariable element ratio per particle. Harvested control and labeled cells were suspended in growth media and assembled into pellets for 2–3 days to form spheroids of  $\approx 300\,000$  cells (Figure 1D). Cell viability of spheroid-forming cells was measured through immunofluorescence and histological analysis (Figure 1E,F). Histological sections stained with hematoxylin and eosin demonstrated viable and compact tissue in both control and labeled cells (Figure 1F; Figure S4, Supporting Information). In these images, the nano hybrid accumulations appear as black spots that are homogeneously distributed throughout the spheroid with high penetration at the core region. Actin/DAPI staining indicated

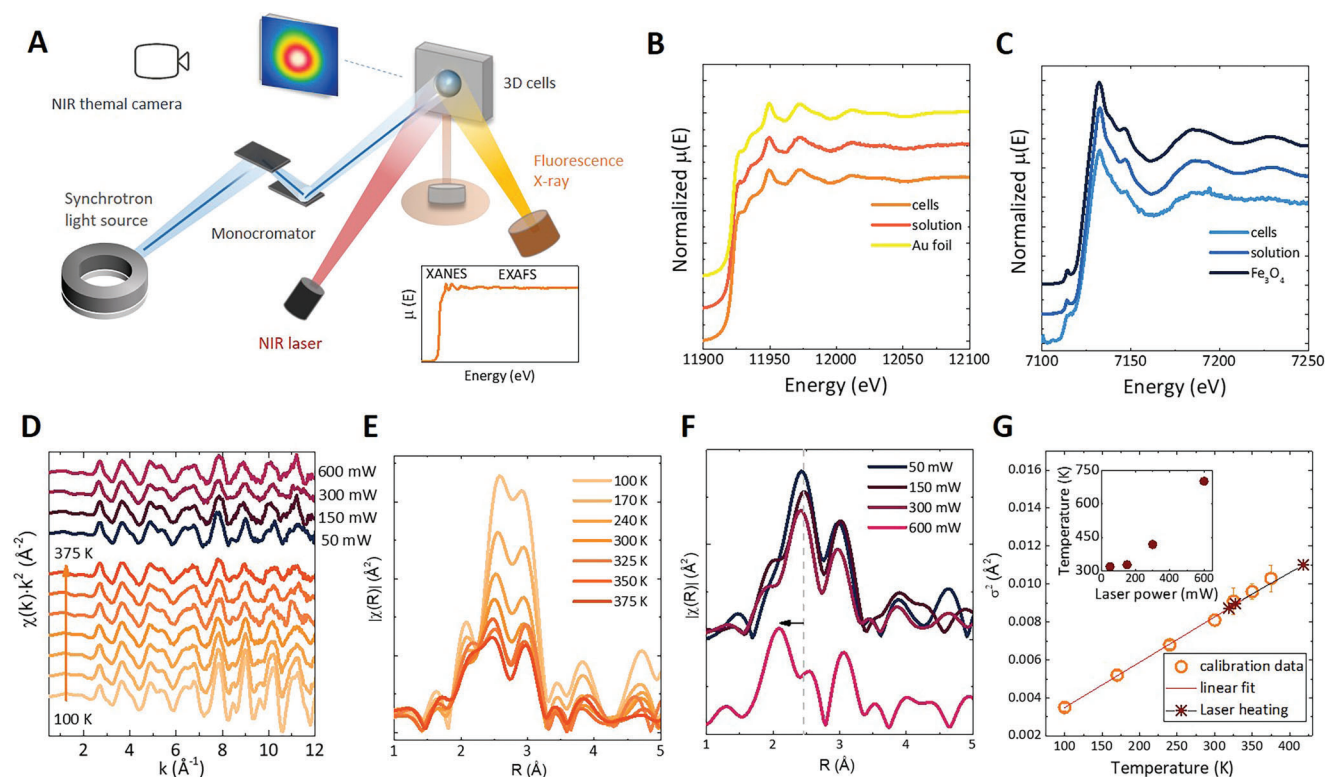


**Figure 2.** A) Scheme of the experimental set-up to obtain X-ray absorption nanothermometry inside cells measurements applying simultaneously X-rays and NIR laser irradiation on systems based on nanoheaters within 3D tumor spheroids. A thermographic camera is positioned in place to monitor the macroscopic temperature achieved under photothermal excitation. B) XANES at both (B) Au  $L_3$ -edge (11 919 eV) and C) Fe K-edge (7112 eV) at 300 K of Au/ $Fe_3O_4$  nanohybrids as-synthesized and in cells. D) Au  $L_3$ -edge EXAFS oscillation functions  $\chi(k) \cdot k^2$  in the calibration range from 100 to 375 K and subjected to photothermal excitation at different density powers (0.05–0.6 W). E, F) Fourier transformed EXAFS signal (FT) in the calibration range (100–375 K) and under photothermal excitation (0.05–0.6 W). G) Temperature-dependent curve of Debye–Waller factor ( $\sigma^2$ ) for nanohybrids (calibration fit curve) (open symbols). The solid symbols correspond to calculated values under photothermal excitation. The solid lines represent the fitting following the Debye–Einstein model in the linear approximation (100–375 K). Inset: Local temperatures attained under laser excitation (0.05–0.6 W).

gathering proliferative cells at the surface and core of the tumor spheroid characteristic of cohesive and collagen-rich ECM as depicted in Figure 1E.

## 2.2. Preservation of Photothermal Properties of Gold and Iron-Oxide Nanohybrids in 3D Tumor Spheroids

Magnetic and plasmonic features are responsible for the hyperthermic capabilities of Au/ $Fe_3O_4$  nanohybrids revealing high magneto- and photothermal efficiencies of synthesized materials.<sup>[22]</sup> On one hand, the branched gold part of the structure, also known as gold nanostars,<sup>[29–31]</sup> shows a high photothermal conversion efficiency compared to other gold nanoarchitectures.<sup>[32]</sup> On the other hand, iron oxide nanoparticles have also emerged as performant agents for PTT in the NIR biological windows due to a band charge transfer produced by the mixed valence state in certain phases between the iron cations (coexistence of  $Fe^{2+}$  and  $Fe^{3+}$ ) characteristic of magnetite structures ( $Fe_3O_4$ ).<sup>[33]</sup> The superparamagnetic properties and saturation magnetization associated with the iron oxide part of the nanohybrid ( $M_s = 75 \text{ emu g}^{-1}$ ) are maintained in the cell environment (see Figure 1G) despite form-

ing accumulations within the intercellular space, which can lead to an increase of dipole–dipole interactions with reduced magneto-thermal performance.<sup>[34]</sup> Zero-field cooling (ZFC) and field cooling (FC) magnetization curves of nanohybrids in cells are depicted in Figure S5 (Supporting Information). The endosomal capture red-shifts the localized surface plasmon resonances (LSPR) response from the vis–NIR region (600–900 nm) to a wider NIR range (600–1200 nm) useful at the first and second biological transparency window (Figure 1H). This nanoparticle assemblage hence enhances their photothermal capability at the cellular level, turning it out more effective at the therapeutic biological windows where the transmission of NIR light in tissues is maximal.<sup>[30,35]</sup> In this study, we have then focused on the photoinduced temperature effect to investigate nanothermometry of nanoparticles inside cells.

XAS measurements of nanohybrids were first obtained at room temperature to investigate their structure and composition once they have been internalized in cell spheroids. Au/ $Fe_3O_4$  in spheroids were illuminated with X-rays upon synchrotron radiation at the SAMBA beamline (SOLEIL synchrotron, France) at both Au  $L_3$ - and Fe K-edges as it is schematically shown in Figure 2A. A signal was collected in fluorescence mode due to the attenuating characteristics of cell tissue and the diluted

condition of absorbing atoms. The X-ray absorption near-edge structure (XANES) provided direct evidence of metallic Au and magnetite Fe<sub>3</sub>O<sub>4</sub> electronic structure (with charge ordering occupation of Fe<sup>2+</sup> and Fe<sup>3+</sup>) for nanohybrids as-synthesized and in cells (compared with Au bulk metal and Fe<sub>3</sub>O<sub>4</sub> references) (Figure 2B,C). These results together with those of TEM observations (Figure 1C) certify the compositional and structural robustness of these nanohybrids in the intracellular environment.

### 2.3. X-Ray Absorption Spectroscopy (XAS) as a Nanoscale Thermal Probe Inside Cells

Previous experiments have demonstrated that XAS can be used as a precise, versatile, and direct nanothermometric technique to monitor the local temperature of gold-based compounds under NIR laser light at the nanoscale.<sup>[21]</sup> Recent reports have shown the determination of local heating using extended X-ray absorption fine structure (EXAFS) spectroscopy in several inductively thermal systems.<sup>[36,37]</sup> This time the thermoactivated agents will be monitored at the cellular level within the tumor environment, which has never been explored with this technique. Our experimental setup integrates a laser source (808 nm), a thermal infrared camera, and a fluorescence detector to apply photothermal excitation through the simultaneous acquisition of XAS data at *in operando* conditions (Figure 2A). By analyzing the oscillatory EXAFS signal  $\chi(k)$ , the structural and vibrational local parameters can be quantified for a selected element:

$$\chi(k) = \sum_i \frac{(N_i S_0^2) F_i(k)}{k R_i^2} \sin[2k R_i + \delta_i(k)] e^{-2\sigma_i^2 k^2} e^{-2R_i/\lambda(k)} \quad (1)$$

where  $N_i$  is the coordination number of atom  $i$ ,  $R_i$  is the interatomic distance of each shell, and  $\sigma_i^2$  the mean displacement due to thermal motion, also known as the Debye–Waller factor. This is a relevant factor that accounts for the thermal vibrations of atoms ( $\sigma_i^2$ ) and can be modeled following a correlated Debye model equation, which can be approximated to a linear equation at high temperatures (from 50 K):<sup>[38,39]</sup>

$$\sigma_T^2 \sim \frac{A}{\theta_D} \left( \frac{1}{4} + \frac{T}{\theta_D} \right) \quad (2)$$

where  $A$  is a constant containing the mass ( $M$ ) of the atom,  $k_B$  the Boltzmann constant, and  $\theta_D$  the Debye–Einstein temperature. In this experiment, we will monitor the local structure variations related to thermal vibration in Au atoms. We will show that the thermal dependence of  $\sigma_T^2$  is a precise and robust nanothermometer of the system, particularly in metallic materials, such as Au. In the case of these nanohybrids, the EXAFS analysis of metallic Au–Au shells and their scattering paths will provide a more reliable temperature parametrization and measurement compared with the metal–oxygen in oxide compounds. This is mainly due to the much larger strength of the metal–oxide bond. A thermal-dependent experiment  $\sigma_T^2$  versus,  $T$  of Au atoms is initially conducted in a controlled range of induced temperatures (100–375 K) using a He gas exchange cryostat. This aims to determine the thermal dependency function of  $\sigma_i^2$ . Subsequently, the same measurements are performed on nanomaterials sub-

jected to 808 nm laser excitation conditions to resolve the local temperature achieved under photoexcited hyperthermia.

As depicted in Figure 2D, thermal motion modifies the amplitude of the EXAFS signal. Fourier-transformed (FT)  $k^2$ -weighted EXAFS signal of Au/Fe<sub>3</sub>O<sub>4</sub> nanomaterials in cells under different temperatures was transformed using a  $k$ -range of 3–11 Å<sup>-1</sup> (Figure 2E). The collection of a sufficient number of scans and the continuous-scan mode provided a high signal-to-noise ratio during measurements. The EXAFS data were fitted using theoretical phase and amplitude functions using the FEFF8.1 program<sup>[40]</sup> as simulated curves. The analysis calculations were performed employing Artemis software.<sup>[41]</sup>

The FT of the EXAFS signal at the Au L<sub>3</sub>-edge shows two main maxima (not phase-corrected) corresponding to the metallic Au–Au bond distances, which are compared with the EXAFS of the Au foil where the atomic structure is known ( $R_{\text{Au–Au}} = 2.86$  Å and coordination number  $N = 12$ ). The Au–Au nearest-neighbor coordination number ( $N$ ) is slightly reduced by the nanosize effects  $N = 11.5 \pm 1$ . As shown in Figure 2E, the increase in thermal activation and disorder causes a decrease in FT intensities from 100 to 375 K. The fitting of the FT data at different temperatures resulted in the calculation of  $\sigma^2$  and in a linear calibration of temperature-dependent structural parameters of Au atoms (see Table S1, Supporting Information). Analysis of the EXAFS signal of these nanomaterials in solution and cells at both Au L<sub>3</sub>- and Fe K-edges and at 300 K are depicted in Figure S6 (Supporting Information) and also verify the fcc Au and magnetite spinel structural configuration.

Once the calibration curve  $\sigma^2(T)$  is derived, experimental EXAFS spectra of Au/Fe<sub>3</sub>O<sub>4</sub> in cell spheroids under different laser excitation conditions were measured. For this, both X-ray and laser beams were synchronously illuminating the same region in the spheroid sample. The samples were irradiated using an 808 nm laser at different increased irradiation powers (from 0.05 to 0.6 W). The macroscopic temperature increments of the illuminated spheroids were simultaneously monitored at the front of the sample until they reached the steady-state after 15 min. EXAFS spectra and FT were acquired at each irradiation power (Figure 2F). As observed during the previous calibration, thermal oscillations of atoms lead to damping of the EXAFS signal when increasing laser power. For the highest laser power, an additional contribution is observed for the FT signal, while the main two peaks are still distinguishable. The fitting of this EXAFS signal is accomplished by introducing an additional Au–X shell. The best fit is achieved with an Au–X shell distance at  $R = 2.14$  Å, with a mean coordination of 0.3. This value of  $R$  suggests that this new contribution could potentially arise from the formation of Au–O bonds at the Au surface within this temperature range. The EXAFS fitting parameters and Debye–Waller factor values  $\sigma^2$  are extracted (see Table 1) and the local temperature of vibrational atoms in the cell matrix is obtained from the  $\sigma^2$  of the Au–Au first shell (Figure 2G). The measured local temperatures were 318, 327, 419, and 703 K under 0.05, 0.15, 0.3, and 0.6 W power laser conditions. These values correspond to temperature increments of ( $\Delta T$ ) of 23, 32, 123, and 408 °C (see Table 1). The linear dependency of the Debye–Waller factor in the range of temperatures has enough sensitivity to detect the photoinduced heating that nanohybrids undergo. The uncertainties of the temperature measurements are below 4 °C.

**Table 1.** Experimental structural parameters (coordination number (N), the average Au–Au and Au–O bond length (R), and the EXAFS Debye–Waller factor ( $\sigma^2$ ) from EXAFS data of nano hybrids under NIR-laser excitation and the corresponding local temperatures (T (K) and  $\Delta T$  ( $^{\circ}\text{C}$ )).

Laser power [mW]	Shell	N	R	$\sigma^2$ ( $\text{\AA}^2$ )	T [K]	$\Delta T$ [ $^{\circ}\text{C}$ ]
50	Au–Au	11.1 (3)	2.86	0.0087 (2)	318 (4)	23
150	Au–Au	11.1 (3)	2.86	0.0092 (3)	327 (4)	32
300	Au–Au	11.1 (3)	2.85	0.0111 (2)	419 (4)	123
600	Au–Au	11.1 (3)	2.84	0.0179 (5)	703	408
	Au–O	0.3 (3)	2.14	0.0146 (5)	—	—

The appearance of an additional contribution, in this case possibly identified as Au–O, in the EXAFS FT could be attributed to the formation of active surface species on the Au at the highest temperature studied here. This phenomenon has been previously reported to happen in Au nanoparticles/oxide interfaces at enough temperatures.<sup>[42]</sup> To support this, the differential features in the Au  $L_3$ -edge XANES (Figure 2F; Figure S6, Supporting Information) of the nanoparticles under 0.6 W power laser condition just indicate the possible formation of these species at the nanoparticle surface. Here, we report a local temperature increase of 408  $^{\circ}\text{C}$  in the nanoparticles induced by laser radiation, which seems to be enough to activate these types of reactions.

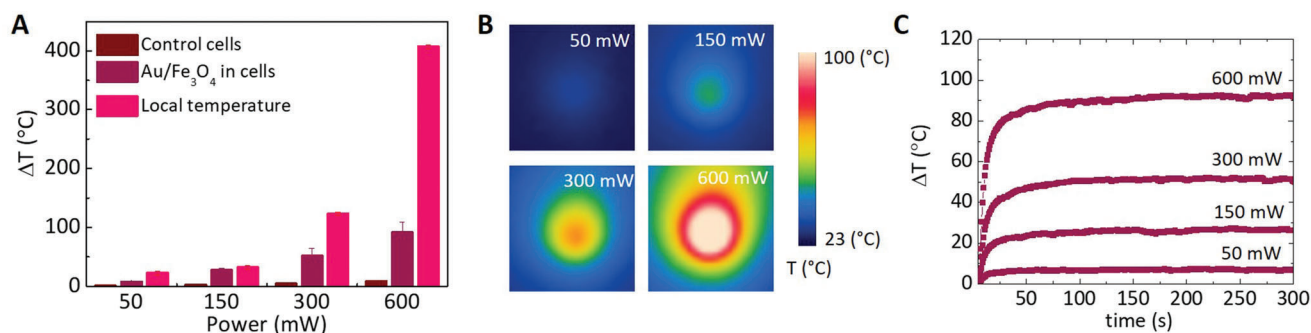
#### 2.4. Global versus Local Photo-induced Heating in Gold-Iron Oxide Nano hybrids in the Tumor Environment

Figure 3A,B shows the thermal increments provided by the infrared thermal camera of control and labeled aggregates subjected to 15 min of laser irradiation (0.05–0.6 W). They are compared with local temperature obtained with the EXAFS nanothermometry method. In all cases, the EXAFS analysis yielded much higher temperature values than those obtained globally. From the lowest to higher power laser, nano hybrids in cells reached macroscopic temperature elevations of  $\Delta T = 7, 27, 51,$  and  $92$   $^{\circ}\text{C}$  as the maximum value. Non-specific heating produced by laser illumination in control cells at different conditions is also depicted in Figure 3A attaining  $\Delta T = 1, 3, 4,$  and  $8$   $^{\circ}\text{C}$ . The difference between the temperature increase at the nanoscale and at the global temperature points out the existence of nanoscale hot regions

around photo-excited nano hybrids. These strong thermal spots are in general two to threefold higher. For the highest power, this divergence can achieve more than four times more intensity.

### 3. Discussion and Conclusion

When comparing both photo-induced global and nanoscale temperatures, the photothermal effect at the core of nano hybrids inside cells is higher than in the surrounding media. This thermal-confined divergence benefits from the bi-composition of the nano hybrid structure. As previously observed, photothermal heating of gold-iron oxide core within a boron nitride matrix resulted in a higher thermal gradient between their surface and the circumambient compared to single gold nanomaterials under the same laser conditions.<sup>[21]</sup> The lowest thermal dissipation of the iron oxide part (in this case, magnetite) can amplify the photoactivated hot areas and act as a thermal storage of the heated system. This can limit the extent of the thermal treatment only to the regions where nanoparticles are located (in cytoplasmic endosomes) and, hence, solely to tumor cells, allowing the preservation of healthy tissues. The variation of Debye–Waller factor with temperature  $\sigma^2(T)$  has demonstrated to be a fine parameter to monitor thermal variations in cells, where it increases from 12% to 24% in the temperature range of 325–375 K from the value at 300 K (see Table S1, Supporting Information). Extracted values from analysis point out parameter differences of  $\sigma^2$  up to 75% when subjected to the highest laser power. Moreover, the Debye–Einstein model in the linear approximation allows using this nanothermometry in a wide range of temperatures covering the region in which the intracellular hyperthermia occurs. The excellent linearity of Debye–Waller factors is extended to temperatures over 500 K in metallic nanoparticles (such as Au,<sup>[39]</sup> Pt,<sup>[37]</sup> or Ag<sup>[43]</sup> nanomaterials). Moreover, EXAFS is directly concentration-independent and exhibits robustness against varying conditions of pH, viscosity, and ionic concentration. This technique is not limited by the diffraction limit used in imaging techniques. The temperature information is restricted to the initial interatomic bonds of Au, providing an average temperature measurement across the X-ray illuminated region, while reflecting the precise local temperature of the embedded gold-based aggregates inside cells. Their application on heated nanosystems in the tumor environment is investigated us-



**Figure 3.** A) Temperature elevations for Au/Fe<sub>3</sub>O<sub>4</sub> subjected to different laser powers (0.05–0.6 W), reaching the thermal steady state, measured with the EXAFS technique (local temperature) and with the infrared thermal camera. The macroscopic temperature increase of control cells (unlabeled) has been also measured upon laser excitation. B,C) Infrared thermal images and temperature curves of Au/Fe<sub>3</sub>O<sub>4</sub> nano hybrids under laser irradiation at different laser powers (0.05–0.6 W).

ing a 3D spheroid that provides a model that can faithfully mimic the *in vivo* scenario. A homogeneous distribution and penetration of nanohybrids in the tumor tissue have been observed. All of the nanohybrids are located in the cytoplasm, making them excellent agents for thermometry inside cells. The nanoscale temperature gradient observed in laser-heated nanoparticles in cells provides compelling evidence that heating is significantly enhanced when nanoparticles are embedded in a cellular matrix. The EXAFS methodology is a reliable and robust tool that provides a means to investigate potentially sharp thermal gradients, which are characteristic of nanoparticle-mediated hyperthermia treatments.

This localized effect on nanometer scales can benefit therapeutic protocols by reducing the intensity of the experimental parameters responsible for oncological doses such as global heating effects in hyperthermia protocols (power laser or external magnetic field), radiotherapy energy, or chemotherapeutic agents while sparing surrounding healthy tissues remain. This nanothermal gradient phenomenon has been already observed in nanosystems upon external stimuli actuation.<sup>[8,11,15,44]</sup> One of the major gains of the present methodology is to combine measurements of both induced heating and thermal sensing on the same nanosystem inside the tissue. Few systems and methodologies have succeeded in the unmediated determination of the local temperature of photo-excited nanoparticles *in vitro* and *in vivo* using luminescent probes.<sup>[45]</sup> The EXAFS methodology applied in the tumor spheroid model allows the creation of *in vitro* cell culture libraries that are directly comparable to animal and patient tissues to explore *in vivo*-like conditions. This nanothermometry method can serve as a valuable complement to other nanoscale thermal sensing tools with higher sensitivities but lower capacity to detect very high thermal gradients at the nanoscale.

This advanced technology can be adapted to any nanomaterials for cellular use to solve biomedical problems. The suitability and versatility of EXAFS nanothermometry demonstrate that it can be implemented in non-biological applications. For instance, it can be utilized for thermal monitoring of chemical elements in microelectronics, catalysis, fuel cells, or in the development of thermochromic materials.<sup>[46]</sup>

In this pioneering study, X-rays act as a probe of the local temperature in the nanomaterials inside tumor-mimicking tissues for the first time, evidencing the existence of nanothermal confined regions due to laser-heated nanoparticles inside cells.

## 4. Experimental Section

**Chemicals:** Hydrogen tetrachloroaurate(III) trihydrate (99.99%, Alfa Aesar), oleylamine (80–90%, Acros Organics), 1-octadecene (90%, Aldrich), oleic acid (90%, Aldrich), iron(0) pentacarbonyl (99.99%, Aldrich), 1,2-hexadecanediol (90%, Aldrich), methoxypolyethylene glycol acetic acid (PEG, 80%,  $M_n = 5000 \text{ g mol}^{-1}$ ), and polyvinylpyrrolidone (PVP,  $M_n = 10\,000$ , Aldrich), were used as received. Additional solvents were reagent grade from Aldrich.

**Gold Nanostars:** Gold nanostars were synthesized by a seed-mediated growth method. Initial gold seeds of  $\approx 14 \text{ nm}$  were synthesized by a modified Turkevich method. 95 mL of 0.5 mM  $\text{HAuCl}_4$  in ultrapure water was heated up and brought to boil. Five milliliters of 1 wt.% of sodium citrate tribasic dehydrate was quickly added under strong stirring and left to react for 15 min. After that, the sample was cooled down and stored in the fridge until further use.

The seed solution was taken from the fridge and left to stir until it reached room temperature. The Au concentration of the seeds solution was measured in a UV-vis spectrometer using an extinction coefficient of  $2.4 \text{ mm}^{-1} \text{ cm}^{-1}$  at a wavelength of 400 nm. A solution of PVP ( $MW 10 \text{ Kg mol}^{-1}$ ) was prepared at  $1 \text{ mg mL}^{-1}$  in water. The amount of PVP added to the solution was calculated to be 60 molecules per  $\text{nm}^2$  of nanoparticle surface. The PVP solution was added dropwise to the nanoparticle solution under mild stirring. The solution was left stirring for 1 h and then centrifuged and redispersed in water two times.

For the synthesis of nanostars, 75 g of PVP ( $MW 10 \text{ Kg mol}^{-1}$ ) was dissolved in 1.5 L of DMF in an Erlenmeyer flask. Once it was completely dissolved, 8.19 mL of  $\text{HAuCl}_4$  50 mM in water was added and left to pre-reduce until all gold passed to  $\text{Au}^+$ , in this case for 5 min.<sup>[29]</sup> The seed solution ( $11.3 \times 10^{-3} \text{ mmol of Au}$ ) was then quickly added and left for a reaction for 2 h. The solution was centrifuged and the supernatant was discarded. The solution was further purified by centrifugation three times in ethanol and finally resuspended in ultrapure water.

**Gold-Iron Oxide Magnetic Nanostars:** Janus magnetic nanostars were synthesized as previously reported.<sup>[23,47]</sup> Its synthesis is based on a seed-mediated-growth process starting with preformed heterodimer seeds of gold/iron oxide with diameters of 15–20 nm. A nanostar growing step was performed in a dimethylformamide solution of chloroauric acid and polyvinylpyrrolidone, following the same procedure as outlined previously. The reaction took place at room temperature, and the nanoparticles were purified by several centrifugation steps and finally resuspended in 40 mL of ultrapure water.

**Cell Culture and Incubation of Nanomaterials:** Human glioblastoma cells (U87) were cultured in a 5%  $\text{CO}_2$  atmosphere at 37 °C with Dulbecco's modified Eagle medium (DMEM) supplemented with 10% fetal bovine serum (FBS), 1% L-glutamine, and 1% penicillin.

The cells were incubated in supplemented DMEM medium for 24 h with different nanoparticle suspensions in T75 flasks at the following concentrations within the extracellular medium:  $[\text{Au}] = 100$  and  $200 \times 10^{-6} \text{ m}$  for gold-iron oxide magnetic nanostars ( $\text{Au/Fe}_3\text{O}_4$ ). After incubation with the nanoparticles, the cells were washed with medium and detached. Cells were counted and divided in 200 000–300 000 cells-dispersed suspensions in 1.5 mL eppendorfs to finally obtain a cell pellet after centrifugation (1000 rpm, 5 min). The pellets were maintained for 2 days at 37 °C with 5%  $\text{CO}_2$  till spherical aggregates were formed. The aggregates were fixed with a 4% paraformaldehyde (PFA) solution for 30 min and washed three times with phosphate-buffered saline (PBS). Then they were stored with PBS.

**Transmission Electron Microscopy:** Transmission electron micrograph (TEM) images were recorded with a JEM1400 Flash (Jeol) (transmission electron microscopy service, CBM-CSIC, Spain) instrument operating at 120 kV. The morphological feature of nanoparticles was analyzed using ImageJ software.

Tumor cells labeled with nanoparticles were washed and fixed with a suspension of 4% paraformaldehyde (PFA) and 2% glutaraldehyde in  $0.1 \text{ mol L}^{-1}$  sodium cacodylate buffer (pH 7.4) for 2 h, then gradually dehydrated in ethanol (30–100%) and stained with 1% osmium tetroxide containing 1.5% potassium cyanoferrate. The samples were embedded in epoxy resin, cut with a microtome in sections, and mounted in grids for analysis.

**Elemental Analysis and Intracellular Quantification (ICP-OES):** The composition and concentration of Fe and Au in solution and cells were analyzed by inductively coupled plasma optical emission spectrometry (ICP-OES) using an Optima 2100 DV PerkinElmer equipment (chemical analysis service, ICMM-CSIC, Spain). Different solutions of nanoparticles were prepared by adding 1 mL of aqua regia (a mixture of  $\text{HNO}_3$ -HCl in a ratio 1:3) and subjected to 80 °C for 1 h. Isotopic standard reference dilutions of Fe and Au were used to perform a quantification analysis of the elements. The sample was then diluted in MilliQ water to have a final volume of 10 mL.

**Cytotoxicity Assay:** U87 cells were incubated for 24 h in 24-well plates with gold nanostars and gold-iron oxide magnetic nanostars at increasing concentrations (from 12.5 to  $100 \mu\text{g}_{\text{TOTAL}} \text{ mL}^{-1}$ ) in a complete DMEM culture medium. A 10% resazurin (Alamar Blue) solution was added to

DMEM medium without red phenol and incubated for 2–3 h. Then part of the solution for each condition was transferred to a 96-well plate. Fluorescence was measured with a 570 nm excitation filter and a 585 nm emission filter in a microplate reader (Bio-Tek Instruments, Inc.). The fluorescence of the DMEM medium with Alamar Blue solution was used as background control. Cell viability was calculated according to the following formula by comparison with control cells:

$$\text{Viability} = \frac{I_{\text{sample}} - I_{\text{resazurin}}}{I_{\text{control}} - I_{\text{resazurin}}} \quad (3)$$

where  $I_{\text{sample}}$  is the fluorescence signal of the sample,  $I_{\text{control}}$  is the fluorescence signal of the reduced form of resazurin (control), and  $I_{\text{resazurin}}$  is the signal from the solution control: the DMEM culture medium supplemented with 10% resazurin.

**UV-vis-NIR Spectroscopy:** Plasmonic properties of solution and cell suspensions were examined using a Cary Spectrometer (Varian) in the 300–1100 nm spectral range. A cell lysate was prepared to separate the endosomes from the nuclei of cells. Cells were resuspended in a lysis buffer containing 250 mM sucrose and 3 mM imidazole. For improving the release of labeled endosomes, a mechanical disruption was forced out with a needle syringe.

**Magnetic Properties:** The magnetic characterization of the samples was performed using a superconducting quantum interference device (SQUID) (Quantum Design, San Diego, USA) at the Magnetism and Magnetic Materials Lab (ICMM-CSIC, Spain). A small volume of nanoparticles suspension was dried in cotton (or Kapton tape for cells) and introduced in a gelatine capsule. Magnetization hysteresis loops at 300 K and thermal dependence of the magnetization of samples were recorded upon zero-field cooling (ZFC) and field cooling (FC) protocols at 100 Oe (8 kA/m).

**X-Ray Absorption Spectroscopy (XAS):** XAS spectra were recorded in fluorescence mode at SAMBA beamline (SOLEIL synchrotron, France) with a multi-element solid-state detector. Samples in aqueous solutions were dried in drops (of a diameter  $\approx 0.5$  cm). Cell samples containing nanoparticles were measured in the form of multicellular aggregates (1–3 per condition). Both were deposited in Kapton films and mounted in standard supports in a motorized stage. XAS spectra were acquired at the Au  $L_3$ -edge (11 919 eV) and the Fe K-edge (7112 eV) at both energy regions (X-ray absorption near edge structure (XANES) and extended X-ray absorption fine structure (EXAFS)). The use of liquid helium-nitrogen cryostat with vacuum/He-gas insulation enabled us to obtain measurements at different temperatures (from 100 to 375 K). The monochromator energy was calibrated with the edge position of both Au and Fe foils. For each NIR-laser condition, 10–15 scan spectra were acquired and averaged to reduce noise beam fluctuations. Data were treated with Athena software<sup>[41]</sup> for a polynomial pre- and post-edge background subtraction. The EXAFS fits were carried out on the  $k^2$ -weighted EXAFS signal Fourier-transformed in the 3–11  $\text{\AA}^{-1}$  range to obtain the radial distribution  $\approx 1.0$ –4.0  $\text{\AA}$  from absorbing atoms (Au and Fe). The analysis calculations were performed employing Artemis software.<sup>[41]</sup>

**Photothermal Excitation Measurements:** Temperature profiles of samples were obtained by placing the aggregates tube at 30 cm of distance from the laser source. Samples were subjected to an 808 nm laser of 1 W maximum power (Roithner Lasertechnik GmbH, Austria). The samples were illuminated by placing an optical attenuator between the laser and the sample, resulting in laser power conditions of 0.05, 0.15, 0.3, and 0.6 W. Measurements were conducted after 15 min of irradiation, reaching a plateau temperature. The thermal increase was measured using an infrared thermal camera (FLIR T540, USA).

**Histological Analysis:** The morphology and viability of spheroids at the single-cell level were examined with histological analysis. Spheroids (control and labeled with nanohybrids) were fixed with phosphate-buffered 10% formalin at pH 7.4, and dehydrated in a series of graded ethanol solutions with increasing concentrations. They were individually placed in histological cassettes and embedded in paraffin. Sections were stained with hematoxylin and eosin for optical microscopy observation. The preparation of the samples was performed at the Histology Facility at CNB-CSIC (Spain).

**Immunofluorescence Staining:** Spheroids were fixed with 4% paraformaldehyde for 1 h at room temperature and washed three times with PBS. They were next incubated overnight at 4 °C in 1 mL of staining solution (blocking solution with 1:1000 of Thermofisher Phalloidin AlexaFluor 488 and 1:300 Invitrogen DAPI). The next day, the samples were rinsed two times with PBS at room temperature, and z-stack sections (maximum 200  $\mu\text{m}$ ) were imaged with 25 $\times$  water immersion objective by confocal microscopy (Leica Microsystems DMi8).

**Statistical Analysis:** All quantitative data were presented as the mean  $\pm$  standard deviation (SD). The sample size for cell viability results was expressed as  $n$ . Statistical analysis was performed using Origin software.

## Supporting Information

Supporting Information is available from the Wiley Online Library or from the author.

## Acknowledgements

This work was supported by the Comunidad de Madrid (2018-T1/IND-1005 (A. E.), 2018-T1/IND-10360, 2022-5A/IND-24234 (A. M-N.), ASAP-CM S2022/BMD-7434 (A. E.) and NanoMagCOST CMS2018/NMT-4321 (J. C.) projects), MICINN (FPI PRE2020-96246 grant (R. L.M.), PID2021-127033OB-C21 (A. E.), RYC2020-029282-I (A. E.), PID2021-126323OA-I00 (A. M-N), PID2019-106099RB-C43/AEI/10.13039/501100011033 (J. R.) projects and CSIC (PIE-20226AT024 (A. E.)). IMDEA Nanociencia acknowledges the “Severo Ochoa” program for Centres of Excellence in R&D (SEV-2016-0686, CEX2020-001039-S). The authors thank Milagros Guerra for TEM preparation at the electron microscopy service at the Centro de Biología Molecular Severo Ochoa (CBMSO, CSIC-UAM Spain), the ICMM-CSIC technical personnel for ICP-OES measurements, and the Histology Facility at CNB-CSIC (Spain) for the histological preparation of biological samples. The authors thank the SAMBA beamline (SOLEIL synchrotron, France) staff for their support during the experiments.

## Conflict of Interest

The authors declare no conflict of interest.

## Data Availability Statement

The data that support the findings of this study are available from the corresponding author upon reasonable request.

## Keywords

nanomedicines, nanothermal therapy, nanothermometry, photothermia, plasmonic nanoparticles, X-ray absorption spectroscopy

Received: June 20, 2023

Revised: July 10, 2023

Published online:

[1] a) M. J. Caterina, M. A. Schumacher, M. Tominaga, T. A. Rosen, J. D. Levine, D. Julius, *Nature* **1997**, 389, 816; b) F. Wang, Y. Han, N. Gu, *ACS Sens.* **2020**, 6, 290.

[2] N. C. Bal, S. K. Maurya, D. H. Sopariwala, S. K. Sahoo, S. C. Gupta, S. A. Shaikh, M. Pant, L. A. Rowland, E. Bombardier, S. A. Goonasekera, *Nat. Med.* **2012**, 18, 1575.



- [3] N. van den Tempel, M. R. Horsman, R. Kanaar, *Int. J. Hyperthermia* **2016**, *32*, 446.
- [4] a) R. E. Rosensweig, *J. Magn. Magn. Mater.* **2002**, *252*, 370; b) H. S. Huang, J. F. Hainfeld, *Int. J. Nanomed.* **2013**, *8*, 2521; c) I. Rubia-Rodríguez, A. Santana-Otero, S. Spassov, E. Tombác, C. Johansson, P. De La Presa, F. J. Teran, M. d. P. Morales, S. Veintemillas-Verdaguer, N. T. Thanh, *Materials* **2021**, *14*, 706.
- [5] X. Huang, P. K. Jain, I. H. El-Sayed, M. A. El-Sayed, *Las. Med. Sci.* **2008**, *23*, 217.
- [6] a) E. Cazares-Cortes, A. Espinosa, J.-M. Guigner, A. Michel, N. Griffete, C. Wilhelm, C. Ménager, *ACS Appl. Mater. Interfaces* **2017**, *9*, 25775; b) L. Beola, L. Asín, R. M. Fratila, V. Herrero, J. M. De La Fuente, V. Grazú, L. Gutiérrez, *ACS Appl. Mater. Interfaces* **2018**, *10*, 44301; c) R. Chen, G. Romero, M. G. Christiansen, A. Mohr, P. Anikeeva, *Science* **2015**, *347*, 1477.
- [7] D. Jaque, F. Vetrone, *Nanoscale* **2012**, *4*, 4301.
- [8] J. G. Ovejero, I. Armenia, D. Serantes, S. Veintemillas-Verdaguer, N. Zeballos, F. López-Gallego, C. Grüttner, J. M. de la Fuente, M. a. d. Puerto Morales, V. Grazu, *Nano Lett.* **2021**, *21*, 7213.
- [9] a) D. Ruiz, B. del Rosal, M. Acebrón, C. Palencia, C. Sun, J. Cabanillas-González, M. López-Haro, A. B. Hungria, D. Jaque, B. H. Juárez, *Adv. Funct. Mater.* **2017**, *27*, 1604629; b) P. Haro-González, L. Martínez-Maestro, I. Martín, J. García-Solé, D. Jaque, *Small* **2012**, *8*, 2652.
- [10] P. Neumann, I. Jakobi, F. Dolde, C. Burk, R. Reuter, G. Waldherr, J. Honert, T. Wolf, A. Brunner, J. H. Shim, *Nano Lett.* **2013**, *13*, 2738.
- [11] a) A. Riedinger, P. Guardia, A. Curcio, M. A. Garcia, R. Cingolani, L. Manna, T. Pellegrino, *Nano Lett.* **2013**, *13*, 2399; b) J. T. Dias, M. Moros, P. del Pino, S. Rivera, V. Grazú, J. M. de la Fuente, *Angew. Chem., Int. Ed.* **2013**, *52*, 11526.
- [12] Y. Zhang, J. Yu, D. J. Birch, Y. Chen, *J. Biomed. Opt.* **2010**, *15*, 020504.
- [13] a) M. Quintanilla, Y. Zhang, L. M. Liz-Marzán, *Chem. Mater.* **2018**, *30*, 2819; b) B. del Rosal, D. Ruiz, I. Chaves-Coira, B. H. Juárez, L. Monge, G. Hong, N. Fernández, D. Jaque, *Adv. Funct. Mater.* **2018**, *28*, 1806088; c) E. Ximendes, R. Marin, Y. Shen, D. Ruiz, D. Gómez-Cerezo, P. Rodríguez-Sevilla, J. Lifante, P. X. Viveros-Méndez, F. Gámez, D. García-Soriano, G. Salas, C. Zalbidea, A. Espinosa, A. Benayas, M. Desco, F. Teran, B. H. Juárez, D. Jaque, *Adv. Mater.* **2021**, *33*, 2100077.
- [14] a) K. Okabe, N. Inada, C. Gota, Y. Harada, T. Funatsu, S. Uchiyama, *Nat. Commun.* **2012**, *3*, 705; b) R. Piñol, J. Zeler, C. D. Brites, Y. Gu, P. Téllez, A. N. Carneiro Neto, T. E. da Silva, R. Moreno-Loshuertos, P. Fernandez-Silva, A. I. Gallego, *Nano Lett.* **2020**, *20*, 6466; c) J. S. Donner, S. A. Thompson, M. P. Kreuzer, G. Baffou, R. Quidant, *Nano Lett.* **2012**, *12*, 2107; d) J.-M. Yang, H. Yang, L. Lin, *ACS Nano* **2011**, *5*, 5067; e) G. Kucsko, P. C. Maurer, N. Y. Yao, M. Kubo, H. J. Noh, P. K. Lo, H. Park, M. D. Lukin, *Nature* **2013**, *500*, 54; f) S. Kiyonaka, T. Kajimoto, R. Sakaguchi, D. Shinmi, M. Omatsu-Kanbe, H. Matsuura, H. Imamura, T. Yoshizaki, I. Hamachi, T. Morii, *Nat. Methods* **2013**, *10*, 1232; g) L. Shang, F. Stockmar, N. Azadfar, G. U. Nienhaus, *Angew. Chem., Int. Ed.* **2013**, *52*, 11154.
- [15] Y. Gu, R. Piñol, R. Moreno-Loshuertos, C. D. Brites, J. Zeler, A. Martínez, G. Maurin-Pasturel, P. Fernández-Silva, J. Marco-Brualla, P. Téllez, R. Cases, R. N. Belsué, D. Bonvin, L. D. Carlos, A. Millán, *ACS Nano* **2023**, *17*, 6822.
- [16] M. Quintanilla, M. Henriksen-Lacey, C. Renero-Lecuna, L. M. Liz-Marzán, *Chem. Soc. Rev.* **2022**, *51*, 4223.
- [17] T. Sugimura, S. Kajimoto, T. Nakabayashi, *Angew. Chem.* **2020**, *132*, 7829.
- [18] S. Faure, N. Mille, S. S. Kale, J. M. Asensio, J. Marbaix, P. Farger, D. Stoian, W. van Beek, P.-F. Fazzini, K. Soulantica, *J. Phys. Chem. C* **2020**, *124*, 22259.
- [19] V. Rieke, in *Interventional Magnetic Resonance Imaging*, Springer, NY, USA **2011**, pp 271.
- [20] M. Barella, I. L. Violi, J. Gargiulo, L. P. Martinez, F. Goschin, V. Guglielmotti, D. Pallarola, S. Schlücker, M. Pilo-Pais, G. P. Acuna, *ACS Nano* **2020**, *15*, 2458.
- [21] A. Espinosa, G. R. Castro, J. Reguera, C. Castellano, J. Castillo, J. Camarero, C. Wilhelm, M. A. García, A. I. Muñoz-Noval, *Nano Lett.* **2021**, *21*, 769.
- [22] A. Espinosa, J. Reguera, A. Curcio, Á. Muñoz-Noval, C. Kuttner, A. Van de Walle, L. M. Liz-Marzán, C. Wilhelm, *Small* **2020**, *16*, 1904960.
- [23] J. Reguera, D. Jiménez De Aberasturi, M. Henriksen-Lacey, J. Langer, A. Espinosa, B. Szczupak, C. Wilhelm, L. M. Liz-Marzán, *Nanoscale* **2017**, *9*, 9467.
- [24] J. E. Perez, I. Nagle, C. Wilhelm, *Biofabrication* **2020**, *13*, 015018.
- [25] A. Díez, M. Rincón-Iglesias, S. Lanceros-Méndez, J. Reguera, E. Lizundia, *Mater. Today Chem.* **2022**, *26*, 101220.
- [26] J. Reguera, T. Flora, N. Winckelmans, J. C. Rodríguez-Cabello, S. Bals, *Nanoscale Adv* **2020**, *2*, 2525.
- [27] J. N. Israelachvili, in *Intermolecular and Surface Forces*, Academic Press, Cambridge, USA **2011**.
- [28] a) H. Lu, M. H. Stenzel, *Small* **2018**, *14*, 1702858; b) F. Mazuel, A. Espinosa, G. Radtke, M. Bugnet, S. Neveu, Y. Lalatonne, G. A. Botton, A. Abou-Hassan, C. Wilhelm, *Adv. Funct. Mater.* **2017**, *27*, 201770051; c) G. Mary, B. Malgras, J. E. Perez, I. Nagle, N. Luciani, C. Pimpie, A. Asnacios, M. Pocard, M. Reffay, C. Wilhelm, *Cancers* **2022**, *14*, 366; d) R. Gupta, D. Sharma, *Nanoscale Adv.* **2021**, *3*, 3663.
- [29] S. Barbosa, A. Agrawal, L. Rodríguez-Lorenzo, I. Pastoriza-Santos, R. A. Alvarez-Puebla, A. Kornowski, H. Weller, L. M. Liz-Marzán, *Langmuir* **2010**, *26*, 14943.
- [30] A. Espinosa, A. K. Silva, A. Sánchez-Iglesias, M. Grzelczak, C. Péchoux, K. Desboeufs, L. M. Liz-Marzán, C. Wilhelm, *Adv. Health. Mater.* **2016**, *5*, 1040.
- [31] P. S. Kumar, I. Pastoriza-Santos, B. Rodríguez-Gonzalez, F. J. G. De Abajo, L. M. Liz-Marzán, *Nanotechnology* **2007**, *19*, 015606.
- [32] a) K. Jiang, D. A. Smith, A. Pinchuk, *J. Phys. Chem. C* **2013**, *117*, 27073; b) C. Bi, J. Chen, Y. Chen, Y. Song, A. Li, S. Li, Z. Mao, C. Gao, D. Wang, H. Möhwald, *Chem. Mater.* **2018**, *30*, 2709.
- [33] a) J. Tang, M. Myers, K. A. Bosnick, L. E. Brus, *J. Phys. Chem. B* **2003**, *107*, 7501; b) A. Espinosa, R. Di Corato, J. Kolosnjaj-Tabi, P. Flaud, T. Pellegrino, C. Wilhelm, *ACS Nano* **2016**, *10*, 2436; c) S. Cabana, A. Curcio, A. Michel, C. Wilhelm, A. Abou-Hassan, *Nanomaterials* **2020**, *10*, 1548; d) E. Bertuit, E. Benassai, G. Mériguet, J.-M. Greneche, B. Baptiste, S. Neveu, C. Wilhelm, A. Abou-Hassan, *ACS Nano* **2021**, *16*, 271.
- [34] a) R. Di Corato, A. Espinosa, L. Lartigue, M. Tharaud, S. Chat, T. Pellegrino, C. Ménager, F. Gazeau, C. Wilhelm, *Biomaterials* **2014**, *35*, 6400; b) D. Cabrera, A. Coene, J. Leliaert, E. J. Artés-Ibáñez, L. Dupré, N. D. Telling, F. J. Teran, *ACS Nano* **2018**, *12*, 2741.
- [35] A. Plan Sangnier, A. Van de Walle, R. Aufaure, M. Fradet, L. Motte, E. Guénin, Y. Lalatonne, C. Wilhelm, *Adv. Biosyst.* **2020**, *4*, 1900284.
- [36] a) B. Van de Broek, D. Grandjean, J. Trekker, J. Ye, K. Verstreken, G. Maes, G. Borghs, S. Nikitenko, L. Lagae, C. Bartic, *Small* **2011**, *7*, 2498; b) D. J. Rosen, S. Yang, E. Marino, Z. Jiang, C. B. Murray, *J. Phys. Chem. C* **2022**, *126*, 3623.
- [37] T. Ano, S. Tsubaki, A. Liu, M. Matsuhsu, S. Fujii, K. Motokura, W.-J. Chun, Y. Wada, *Commun. Chem.* **2020**, *3*, 86.
- [38] Z. Duan, Y. Li, J. Timoshenko, S. T. Chill, R. M. Anderson, D. F. Yancey, A. I. Frenkel, R. M. Crooks, G. Henkelman, *Catal. Sci. Technol.* **2016**, *6*, 6879.
- [39] G. Shafai, M. A. Ortigoza, T. S. Rahman, *J. Phys.: Condens. Matter* **2012**, *24*, 104026.
- [40] J. J. Rehr, R. C. Albers, *Rev. Mod. Phys.* **2000**, *72*, 621.
- [41] B. Ravel, M. Newville, *J. Synchrotron. Radiat.* **2005**, *12*, 537.
- [42] a) X.-P. Fu, L.-W. Guo, W.-W. Wang, C. Ma, C.-J. Jia, K. Wu, R. Si, L.-D. Sun, C.-H. Yan, *J. Am. Chem. Soc.* **2019**, *141*, 4613; b) Y. Zhou, H. C. Zeng, *J. Phys. Chem. C* **2016**, *120*, 29348.

- [43] M. Dubiel, J. Haug, H. Kruth, H. Hofmeister, W. Seifert, *J. Phys.: Conf. Ser.* **2009**, 190, 012123.
- [44] a) P. L. Silva, O. A. Savchuk, J. Gallo, L. García-Hevia, M. Bañobre-López, J. B. Nieder, *Nanoscale* **2020**, 12, 21647; b) R. Pinol, C. D. Brites, R. Bustamante, A. Martínez, N. J. Silva, J. L. Murillo, R. Cases, J. Carrey, C. Estepa, C. Sosa, *ACS Nano* **2015**, 9, 3134.
- [45] a) Y. Shen, H. D. Santos, E. C. Ximendes, J. Lifante, A. Sanz-Portilla, L. Monge, N. Fernandez, I. Chaves-Coira, C. Jacinto, C. D. Brites, L. D. Carlos, A. Benayas, M. C. Iglesias-de la Cruz, D. Jaque, *Adv. Funct. Mater.* **2020**, 30, 2002730; b) E. C. Ximendes, U. Rocha, K. U. Kumar, C. Jacinto, D. Jaque, *Appl. Phys. Lett.* **2016**, 108, 253103.
- [46] a) Y. Avenas, L. Dupont, Z. Khatir, *IEEE Trans. Power Electron.* **2011**, 27, 3081; b) A. I. Juez, F. Fresno, J. M. Coronado, J. Highfield, A. M. Ruppert, N. Keller, *Curr. Opin. Green Sustain. Chem.* **2022**, 37, 100652; c) E. Resines-Urien, M. Á. G. García-Tuñón, M. García-Hernández, J. A. Rodríguez-Velamazán, A. Espinosa, J. S. Costa, *Adv. Sci.* **2022**, 9, 2270150.
- [47] H. Yu, M. Chen, P. M. Rice, S. X. Wang, R. White, S. Sun, *Nano Lett.* **2005**, 5, 379.